Dynamic modelling and small-signal analysis of an efficient bridge-type multi-input DC converter for hybrid low-power systems

Baya Reddy Lomada[1,2], Vangala Naga Bhaskar Reddy[3]

[1]Department of Electrical & Electronics Engineering, Jawaharlal Nehru Technological University, Anantapur, India
[2]Department of Electrical & Electronics Engineering, Annamacharya Institute of Technology and Science, Rajampet, India
[3]Department of Electrical & Electronics Engineering, Rajeev Gandhi Memorial College of Engineering and Technology, Nandyal, India

Article Info	ABSTRACT
	This paper presents the dynamic modelling and small-signal analysis of a bridge-type multi-input DC converter designed for hybrid low-power systems. The converter architecture supports the integration of multiple energy sources such as fuel cells and photovoltaic (PV) arrays, enabling enhanced flexibility and reliability. A CUK-based configuration is employed to achieve continuous input current and reduced voltage stress across the switches. The dynamic behavior of the converter is analyzed through average large-signal and small-signal state-space modelling. Stability is assessed using the Routh-Hurwitz criterion, and steady-state analysis is carried out to support performance evaluation. Experimental results obtained from a 250 W prototype confirm the validity of the developed models and demonstrate the efficiency and suitability of the proposed converter for hybrid renewable energy systems. *This is an open access article under the <u>CC BY-SA</u> license.*

Corresponding Author:

Baya Reddy Lomada
Department of Electrical & Electronics Engineering, Jawaharlal Nehru Technological University
Anantapur, India
Email: reddy.baya@gmail.com

1. INTRODUCTION

A surplus of energy sources is being exploited to meet the rising power demand [1]-[3]. The world's expanding need for electricity can no longer be met by traditional energy sources since they are quickly running out [4]. The use of natural fuels for energy production also has a detrimental effect on the environment, raising concerns about things like air pollution and global warming [5]. The output of electricity derived from renewable energy sources is consequently rising swiftly, particularly in distributed generation [6]. Thus, developing hybrid energy plans that continuously supply power to the right demand through a variety of green technologies is crucial [7].

The huge majority of electric vehicles (EVs) are battery powered, which depends on two important variables: the availability of lithium and the state of the electricity network today [8]. To avoid the aforementioned issues, research and tests on fuel cell-based cars, photovoltaic, and fuel cell hybrid electric cars must be carried out concurrently [9]. For such cars, the paucity of lithium and the contemporary power grid are irrelevant. Hydrogen is best compared to batteries in terms of both energy density and power density [10]–[12]. Due to the high cost of hydrogen, combining fuel cells with photovoltaic (PV) panels offers a practical way to minimize hydrogen usage in vehicles [13], [14]. As shown in Figure 1, the solar PV, fuel cell, inverter, multi-input DC-DC converter & electric motor comprise the primary powertrain components of a hybrid electric vehicle (HEV). A multi-input DC-DC converter has a substantial impact on the overall stability

and functionality of the HEV powertrain system. Experts have created many multi-input converters MICs), but not all of them are appropriate for every application compared to non-isolated MICs; other types of MICs are far less useful for slight and medium-powered HEVs.
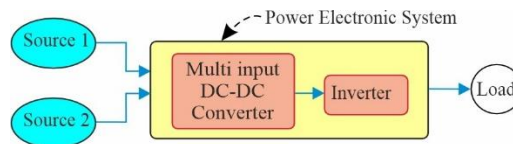

Figure 1. Block diagram of MIC-based HEV

A novel MIC configuration developed with the basic single-ended primary-inductor converter (SEPIC) was presented by the researchers in [15]. It is feasible to integrate many inputs, but at least one of them must be a rechargeable battery. Regretfully, there is a great deal of voltage stress on the switching electronics. A unique MIC structure is described in [16] to integrate the super-capacitor and rechargeable battery for EVs. Relays are used in this converter to carry out the required function no need for any additional circuitry for one input can feed the other, which comparatively increases the circuit difficulty. In Experts in [17]. The authors of [18] introduced a novel type of MIC bridge for establishing connections between many renewable energy sources. To get a larger gain, fewer unidirectional and bidirectional semiconductor switches are used. As more switches are engaged in different operating modes, the electrical stress on each switch tends to increase. This setup also causes a reversal in voltage polarity between the input and the output. A system supporting bidirectional power flow was presented by the researchers in [19]. This work is primarily focused on calculating critical inductance and minimizing voltage ripple. Although there are more switching components and a battery input required, this converter can give electricity in both directions. The development and analysis of a MIC are shown in the article [20]. Reducing the number of Components and the stress on the switch voltage are the converter's key concerns. Unfortunately, there are more losses in this converter, and there are still a lot of components. In [21], A unique modular MIC was suggested by the researchers. It has slight components, a smaller amount of voltage stress, and a better voltage gain. Nevertheless, there are really more parts in this converter, and several switches are under more voltage stress. It also uses more storage components for a multi-input system, which complicates control design and system analysis. In [22], A non-isolated MIC for renewable energy systems (RES) was presented by the authors. Due to the non-coupled inductor, this converter shows greater gain in voltage at a lower component count. In [23], a novel multi-input, high-gain, non-isolated DC converter is presented that features a compact design with a reduced number of components. The use of a single diode facilitates bidirectional power transfer, contributing to both component minimization and enhanced voltage gain. A recent study on dual-input non-isolated converters using sliding mode control for electric vehicle applications demonstrates the potential of such configurations to achieve improved voltage gain and dynamic response [24]. This further supports the applicability of the proposed converter in similar low-power EV systems.

2. PROPOSED CONVERTER

The working principle of the MIC and traditional converters is quite similar. In both cases, the inductive and capacitive components of the converter charge for a predetermined amount of time and then discharge through a load for the rest of the time. The operating technique is the same in the suggested converter. Figure 2 illustrates the recently built multi-input DC power converter intended for HEV use.

2.1. Modes of operation

Figure 3 shows the equivalent circuitry for the six modes of operation of the proposed converter. Fuel cell voltage is V_1, the solar panel output voltage is V_2, S_1 to S_4 are the four MOSFET switches, D is the diode, R is the load resistance, two inductors are L_1 and L_2, and two capacitors are C_1 and C_2. i_{C1}, i_{C2} and i_{L1}, i_{L2} are the respective currents flowing through C_1, C_2 and L_1, L_2. v_{C1}, v_{C2}, v_{L1} and v_{L2} are the respective large signal voltages across C_1, C_2 and L_1, L_2. i_0 and v_0 are the large signal current and voltage, respectively, at the load resistance. T denotes the time period of the gating signal for switch one, while the corresponding large-signal duty cycle values for Modes 1 through 5 are represented by δ_1 to δ_5.
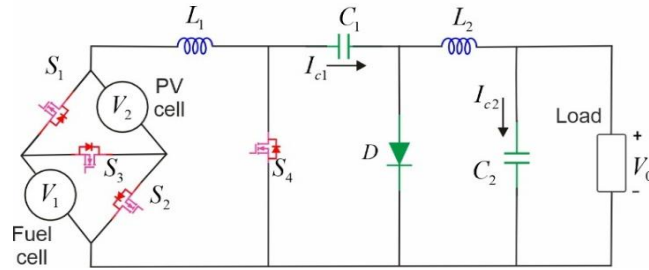
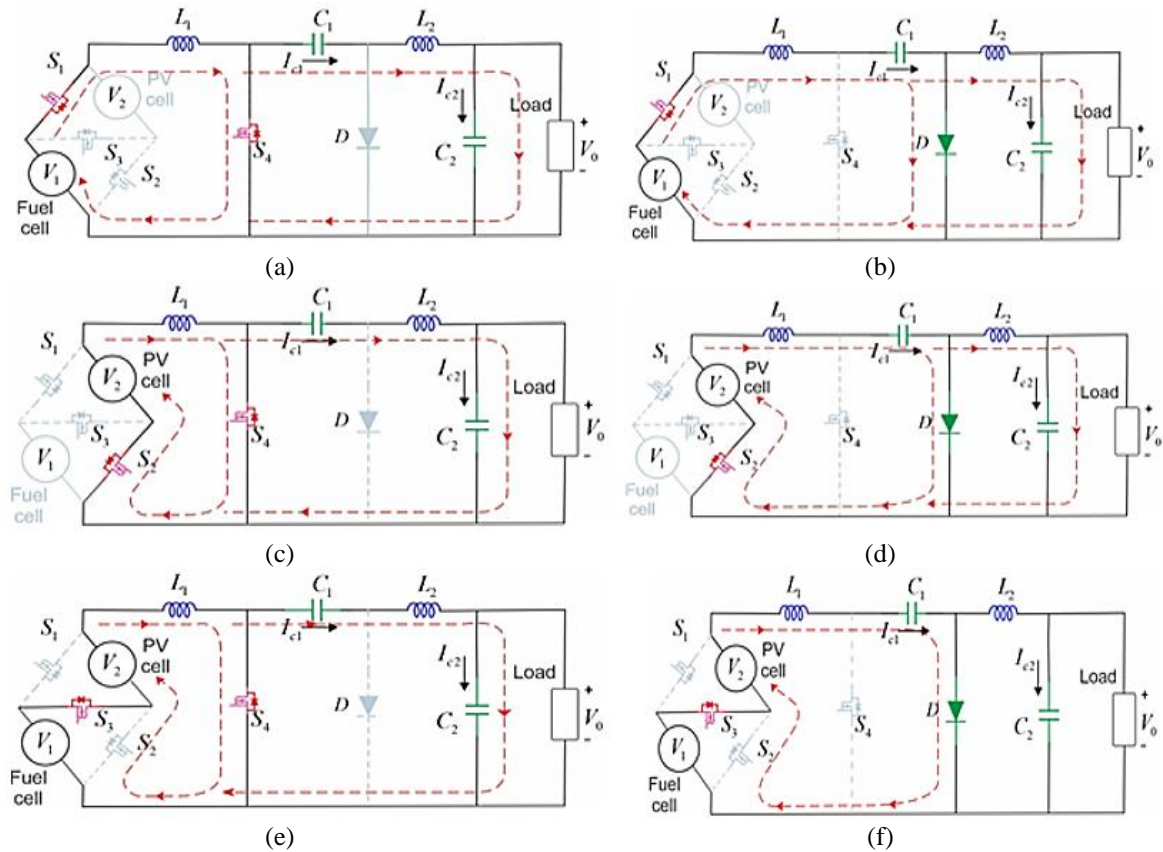Figure 2. Shows the proposed multi-input DC power converter's structure

Figure 3. The proposed converter's modes of operation: (a) mode 1, (b) mode 2, (c) mode 3,
(d) mode 4, (e) mode 5, and (f) mode 6

2.1.1 First mode

In the mode-1 S_1, S_4 are ON state and S_2, S_3, and D is OFF state. Figure 3(a) shows the first mode equivalent circuit. The dynamic equations for the first mode are:

$$\frac{di_{L1}}{dt} = \frac{v_1}{L_1}$$

$$\frac{di_{L2}}{dt} = -\frac{v_{C1}}{L_2} - \frac{v_{C2}}{L_2}$$

$$\frac{dv_{C1}}{dt} = \frac{i_{L2}}{C_1}$$

$$\frac{dv_{C2}}{dt} = \frac{i_{L2}}{C_2} - \frac{v_0}{RC_2}$$

$$v_0 = v_{C2}$$

Since there are four energy storage components in the system, the state variables are i_{L1}, i_{L2}, v_{C1} and v_{C2} mode–1 state space model representation is shown (1) and (2).

$$\begin{bmatrix} \frac{di_{L1}}{dt} \\ \frac{di_{L2}}{dt} \\ \frac{dv_{C1}}{dt} \\ \frac{dv_{C1}}{dt} \end{bmatrix} = \begin{bmatrix} 0 & 0 & 0 & 0 \\ 0 & 0 & \frac{-1}{L_2} & \frac{-1}{L_2} \\ 0 & \frac{1}{C_1} & 0 & 0 \\ 0 & \frac{1}{C_2} & 0 & -\frac{1}{RC_2} \end{bmatrix} \begin{bmatrix} i_{L1} \\ i_{L2} \\ v_{C1} \\ v_{C2} \end{bmatrix} + \begin{bmatrix} \frac{1}{L_1} & 0 \\ 0 & 0 \\ 0 & 0 \\ 0 & 0 \end{bmatrix} \begin{bmatrix} v_1 \\ v_2 \end{bmatrix} \qquad (1)$$

$$v_0 = \begin{bmatrix} 0 & 0 & 0 & 1 \end{bmatrix} \begin{bmatrix} i_{L1} \\ i_{L2} \\ v_{C1} \\ v_{C2} \end{bmatrix} \qquad (2)$$

2.1.2. Second mode

In the second mode, the switches S_1, D are in turn ON, and S_2, S_3, and S_4 are in the OFF state, the corresponding circuit under this mode is shown in Figure 3(b). Based on the dynamic equation in the second mode, the state space model representation is shown (3) and (4).

$$\begin{bmatrix} \frac{di_{L1}}{dt} \\ \frac{di_{L2}}{dt} \\ \frac{dv_{C1}}{dt} \\ \frac{dvc2}{dt} \end{bmatrix} = \begin{bmatrix} 0 & 0 & -\frac{1}{L_1} & 0 \\ 0 & 0 & 0 & -\frac{1}{L_2} \\ \frac{1}{C_1} & 0 & 0 & 0 \\ 0 & \frac{1}{C_2} & 0 & -\frac{1}{RC_2} \end{bmatrix} \begin{bmatrix} i_{L1} \\ i_{L2} \\ v_{C1} \\ v_{C2} \end{bmatrix} + \begin{bmatrix} \frac{1}{L_1} & 0 \\ 0 & 0 \\ 0 & 0 \\ 0 & 0 \end{bmatrix} \begin{bmatrix} v_1 \\ v_2 \end{bmatrix} \qquad (3)$$

$$v_0 = \begin{bmatrix} 0 & 0 & 0 & 1 \end{bmatrix} \begin{bmatrix} i_{L1} \\ i_{L2} \\ v_{C1} \\ v_{C2} \end{bmatrix} \qquad (4)$$

2.1.3. Third mode

In this mode, S2, S4 are ON, and D, and S1 and S3 OFF state. Figure 3(c) shows the equivalent circuit. This mode inductors start charging, v1/L1 and $-\frac{v_{C1}}{L_2} - \frac{v_{C2}}{L_2}$ are the slopes of iL1 and iL2. The flow of inductor current iL1 meets its iL1max2 from its $i_{L1\,min\,2}$ least value. The flow of inductor current iL2 meets its iL2max from its iL2min. C1 starts dis-charging through L2, the slope vc1 is iL2/C1. The capacitor C2 starts energizing the slope of vc2 is $\frac{i_{L2}}{C_2} - \frac{v_{C2}}{RC_2}$. Below are the state-space model equations based on the dynamic equations.

$$\begin{bmatrix} \frac{di_{L1}}{dt} \\ \frac{di_{L2}}{dt} \\ \frac{dv_{C1}}{dt} \\ \frac{dv_{C1}}{dt} \end{bmatrix} = \begin{bmatrix} 0 & 0 & 0 & 0 \\ 0 & 0 & -\frac{1}{L_2} & -\frac{1}{L_2} \\ 0 & \frac{1}{C_1} & 0 & 0 \\ 0 & \frac{1}{C_2} & 0 & -\frac{1}{RC_2} \end{bmatrix} \begin{bmatrix} i_{L1} \\ i_{L2} \\ v_{C1} \\ v_{C2} \end{bmatrix} + \begin{bmatrix} 0 & \frac{1}{L_1} \\ 0 & 0 \\ 0 & 0 \\ 0 & 0 \end{bmatrix} \begin{bmatrix} v_1 \\ v_2 \end{bmatrix} \qquad (5)$$

$$v_0 = \begin{bmatrix} 0 & 0 & 0 & 1 \end{bmatrix} \begin{bmatrix} i_{L1} \\ i_{L2} \\ v_{C1} \\ v_{C2} \end{bmatrix} \qquad (6)$$

2.1.4. Fourth mode

In the fourth mode, S_2, D are ON and S_1, S_3, and S_4 are OFF state, Figure 3(d) shows the equivalent circuit. Inductors L_1 and L_2 start discharging, the slope of i_{L1} and i_{L2} are $\frac{v_2 - v_{C1}}{L_1}$ and $-\frac{v_{C2}}{L_2}$. The i_{L1} reaches to

its i_{L1min3} and i_{L2} meets to i_{L2min}. The capacitors start energizing by v_2, L_1 and L_2, the slopes of v_{c1} and v_{c2} are $\frac{i_{L1}}{C_1}$ and $\frac{i_{L2}}{C_2} - \frac{v_{c1}}{RC_2}$. state-space model derived from the dynamic equations in the fourth mode is below.

$$\begin{bmatrix} \frac{di_{L1}}{dt} \\ \frac{di_{L2}}{dt} \\ \frac{dv_{C1}}{dt} \\ \frac{dv_{C1}}{dt} \end{bmatrix} = \begin{bmatrix} 0 & 0 & -\frac{1}{L_1} & 0 \\ 0 & 0 & 0 & -\frac{1}{L_2} \\ \frac{1}{C_1} & 0 & 0 & 0 \\ 0 & \frac{1}{C_2} & 0 & -\frac{1}{RC_2} \end{bmatrix} \begin{bmatrix} i_{L1} \\ i_{L2} \\ v_{C1} \\ v_{C2} \end{bmatrix} + \begin{bmatrix} 0 & \frac{1}{L_1} \\ 0 & 0 \\ 0 & 0 \\ 0 & 0 \end{bmatrix} \begin{bmatrix} v_1 \\ v_2 \end{bmatrix} \tag{7}$$

$$v_0 = \begin{bmatrix} 0 & 0 & 0 & 1 \end{bmatrix} \begin{bmatrix} i_{L1} \\ i_{L2} \\ v_{C1} \\ v_{C2} \end{bmatrix} \tag{8}$$

2.1.5. Fifth mode

In the fifth mode, S_3, S_4 are ON and S_1, S_2, and D are OFF state. Figure 3(e) shows the equivalent circuit. State-space model derived from dynamic equations in the fourth mode.

$$\begin{bmatrix} \frac{di_{L1}}{dt} \\ \frac{di_{L2}}{dt} \\ \frac{dv_{C1}}{dt} \\ \frac{dv_{C1}}{dt} \end{bmatrix} = \begin{bmatrix} 0 & 0 & 0 & 0 \\ 0 & 0 & \frac{-1}{L_2} & \frac{-1}{L_2} \\ 0 & \frac{1}{C_1} & 0 & 0 \\ 0 & \frac{1}{C_2} & 0 & -\frac{1}{RC_2} \end{bmatrix} \begin{bmatrix} i_{L1} \\ i_{L2} \\ v_{C1} \\ v_{C2} \end{bmatrix} + \begin{bmatrix} \frac{1}{L_1} & \frac{1}{L_1} \\ 0 & 0 \\ 0 & 0 \\ 0 & 0 \end{bmatrix} \begin{bmatrix} v_1 \\ v_2 \end{bmatrix} \tag{9}$$

$$v_0 = \begin{bmatrix} 0 & 0 & 0 & 1 \end{bmatrix} \begin{bmatrix} i_{L1} \\ i_{L2} \\ v_{C1} \\ v_{C2} \end{bmatrix} \tag{10}$$

2.1.6. Sixth mode

In sixth mode, S_3, D are ON and S_1, S_2, and S_4 are OFF state. Figure 3(f) shows the equivalent circuit. The L_1 and L_2 start dis-charging, $\frac{v_1+v_2-v_{c1}}{L_1}$ and $\frac{-v_{c2}}{C_1}$ are the respective slopes of i_{L1} and i_{L2}. The i_{L1} meets to its $i_{L1min4} = i_{L1min1}$ and i_{L2} meets to i_{L2min}. The capacitors starts-charging through V_1, V_2, L_1 and L_2 and slopes of the capacitor voltages v_{c1} and v_{c2} are $\frac{i_{L1}}{C_1}$ and $\frac{i_{L2}}{C_2} - \frac{v_{c2}}{RC_2}$. The state-space model derived from the dynamic equations in the fourth mode is below.

$$\begin{bmatrix} \frac{di_{L1}}{dt} \\ \frac{di_{L2}}{dt} \\ \frac{dv_{C1}}{dt} \\ \frac{dv_{C1}}{dt} \end{bmatrix} = \begin{bmatrix} 0 & 0 & -\frac{1}{L_1} & 0 \\ 0 & 0 & 0 & -\frac{1}{L_2} \\ \frac{1}{C_1} & 0 & 0 & 0 \\ 0 & \frac{1}{C_2} & 0 & -\frac{1}{RC_2} \end{bmatrix} \begin{bmatrix} i_{L1} \\ i_{L2} \\ v_{C1} \\ v_{C2} \end{bmatrix} + \begin{bmatrix} \frac{1}{L_1} & \frac{1}{L_1} \\ 0 & 0 \\ 0 & 0 \\ 0 & 0 \end{bmatrix} \begin{bmatrix} v_1 \\ v_2 \end{bmatrix} \tag{11}$$

$$v_0 = \begin{bmatrix} 0 & 0 & 0 & 1 \end{bmatrix} \begin{bmatrix} i_{L1} \\ i_{L2} \\ v_{C1} \\ v_{C2} \end{bmatrix} \tag{12}$$

2.2. Modeling of average-large signal

The switches used in the proposed converter introduce nonlinear behaviour, resulting in a circuit that does not follow linear system dynamics. To effectively represent this behaviour, average large-signal modelling is applied. This method captures the influence of switching actions and practical voltage sources, providing a close approximation of the converter's actual performance under operating conditions.

The corresponding state-space model for the average large-signal representation is given in (13) to (15). In this model, the direct transmission matrix D is zero, indicating that the output does not directly depend on the instantaneous input. These equations derive from (1)-(12).

$$A = \begin{bmatrix} 0 & 0 & 0 & 0 \\ 0 & 0 & \frac{-1}{L_2} & \frac{-1}{L_2} \\ 0 & \frac{1}{C_1} & 0 & 0 \\ 0 & \frac{1}{C_2} & 0 & -\frac{1}{RC_2} \end{bmatrix} (\delta_1 + \delta_3 + \delta_5) + \begin{bmatrix} 0 & 0 & -\frac{1}{L_1} & 0 \\ 0 & 0 & 0 & -\frac{1}{L_2} \\ \frac{1}{C_1} & 0 & 0 & 0 \\ 0 & \frac{1}{C_2} & 0 & -\frac{1}{RC_2} \end{bmatrix} (1 - \delta_1 - \delta_3 - \delta_5) \quad (13)$$

$$B = \begin{bmatrix} \frac{1}{L_1}(1 - \Delta_3 - \Delta_4) & \frac{1}{L_1}(1 - \Delta_1 - \Delta_2) \\ 0 & 0 \\ 0 & 0 \\ 0 & 0 \end{bmatrix} \quad (14)$$

$$C = \begin{bmatrix} 0 & 0 & 0 & 1 \end{bmatrix} \quad (15)$$

2.3. Small-signal modeling

Small-signal analysis is used to approximate the nonlinear behaviour of the converter by expressing each variable as the sum of its steady-state value and a small variation. To develop the small-signal model of the proposed converter, slight deviations are introduced in the input voltages, duty ratios, and state variables. The method of deriving the small-signal model and analysing system stability follows fundamental techniques widely used in power electronics, as detailed in classical converter design references [25]. This method simplifies the dynamic equations, making them suitable for linear system analysis and control system design.

$$v_1 = V_1 + \hat{v}_1$$

$$v_2 = V_2 + \hat{v}_2$$

$$i_{L1} = I_{L1} + \hat{i}_{L1}$$

$$i_{L2} = I_{L2} + \hat{i}_{L2}$$

$$v_{C1} = V_{C1} + \hat{v}_{C1}$$

$$v_{C2} = V_{C2} + \hat{v}_{C2}$$

$$\delta_1 = d_1 + \hat{\delta}_1$$

$$\delta_2 = d_2 + \hat{\delta}_2$$

$$\delta_3 = d_3 + \hat{\delta}_3$$

$$\delta_4 = d_4 + \hat{\delta}_4$$

$$\delta_5 = d_5 + \hat{\delta}_5$$

Where, V_1 and V_2 are the fuel cell voltage and solar panel voltage under steady state. I_{L1} and I_{L2} are the current flowing through L_1 and L_2 respectively. The respective V_{C1} and V_{C2} are the final state voltages across C_1 and C_2. d_1 to d_2 are the duty ratios of first Mode to fifth Mode respectively. $\hat{v}_1$ and $\hat{v}_2$ are the fuel cell voltage and solar panel voltage (perturbation component). $\hat{i}_{L1}$ and $\hat{i}_{L2}$ are the small signal currents of L_1 and L_2. $\hat{v}_{C1}$ and $\hat{v}_{C2}$ are the small signal voltages across C_1 and C_2. $\hat{\delta}_1$ to $\hat{\delta}_5$ are the respective small-signal duty ratios of first mode to fifth mode. Include small signal components in (13) to (15).

$$\frac{di_{L1}}{dt} + \frac{d\hat{i}_{L1}}{dt} = -\frac{1}{L_1}\left(1 - (d_1 + \hat{\delta}_1) - (d_3 + \hat{\delta}_3) - (d_5 + \hat{\delta}_5)\right)(V_{C1} + \hat{v}_{C1}) + \frac{1}{L_1}\left(1 - (d_3 + \hat{\delta}_3) - (d_4 + \hat{\delta}_4)\right)(V_1 + \hat{v}_1) + \frac{1}{L_1}\left(1 - (d_1 + \hat{\delta}_1) - (d_2 + \hat{\delta}_2)\right)(V_2 + \hat{v}_2) \quad (16)$$

Separate the perturbation component term from equation (16), and assume that higher order terms are zero.

$$\frac{d\hat{\imath}_{L1}}{dt} = -\frac{1}{L_1}\Big((1 - d_1 - d_3 - d_5)\hat{v}_{C1} - (1 - d_3 - d_4)\hat{v}_1 - (1 - d_1 - d_2)\hat{v}_2 + (-V_{C1} - V_2)\hat{\delta}_1 +$$
$$V_2\hat{\delta}_2 + (-V_{C1} - V_1)\hat{\delta}_3 + V_1\hat{\delta}_4 + (-V_{C1})\hat{\delta}_5\Big) \tag{17}$$

Similarly,

$$\frac{d\hat{\imath}_{L2}}{dt} = -\frac{1}{L_2}\Big((d_1 + d_3 + d_5)\hat{v}_{C1} + \hat{v}_{C2} + (V_{C1})\hat{\delta}_1 + (V_{C1})\hat{\delta}_3 + (V_{C1})\hat{\delta}_5\Big) \tag{18}$$

$$\frac{d\hat{v}_{C1}}{dt} = \frac{1}{C_1}\Big((1 - d_1 - d_3 - d_5)\hat{\imath}_{L1} + (d_1 + d_3 + d_5)\hat{\imath}_{L2} - (I_{L1} + I_{L2})\hat{\delta}_1 - (I_{L1} + I_{L2})\hat{\delta}_3 -$$
$$(I_{L1} + I_{L2})\hat{\delta}_5\Big) \tag{19}$$

$$\frac{d\hat{v}_{C2}}{dt} = \frac{1}{C_2}\hat{\imath}_{L2} - \frac{1}{RC_2}\hat{v}_{C2} \tag{20}$$

From the (17) to (20),

$$\begin{bmatrix} \frac{d\hat{\imath}_{L1}}{dt} \\ \frac{d\hat{\imath}_{L2}}{dt} \\ \frac{d\hat{v}_{C1}}{dt} \\ \frac{d\hat{v}_{C2}}{dt} \end{bmatrix} = \begin{bmatrix} 0 & 0 & -\frac{1}{L_1}(1 - d_1 - d_3 - d_5) & 0 \\ 0 & 0 & -\frac{1}{L_2}(d_1 + d_3 + d_5) & -\frac{1}{L_2} \\ \frac{1}{C_1}(1 - d_1 - d_3 - d_5) & \frac{1}{C_1}(d_1 + d_3 + d_5) & 0 & 0 \\ 0 & \frac{1}{C_2} & 0 & -\frac{1}{RC_2} \end{bmatrix} \begin{bmatrix} \hat{\imath}_{L1} \\ \hat{\imath}_{L2} \\ \hat{v}_{C1} \\ \hat{v}_{C2} \end{bmatrix} +$$

$$\begin{bmatrix} -\frac{1}{L_1}(-V_{C1} - V_2) & -\frac{V_2}{L_1} & -\frac{1}{L_1}(-V_{C1} - V_1) & \frac{V_1}{L_1} & -\frac{1}{L_1}(-V_{C1}) & \frac{1}{L_1}(1 - d_3 - d_4) & \frac{1}{L_1}(1 - d_1 - d_2) \\ -\frac{1}{L_2}(V_{C1}) & 0 & -\frac{1}{L_2}(V_{C1}) & 0 & -\frac{1}{L_2}(V_{C1}) & 0 & 0 \\ \frac{1}{C_1}(I_{L2} - I_1) & 0 & \frac{1}{C_1}(I_{L2} - I_1) & 0 & \frac{1}{C_1}(I_{L2} - I_1) & 0 & 0 \\ 0 & 0 & 0 & 0 & 0 & 0 & 0 \end{bmatrix} \begin{bmatrix} \hat{\delta}_1 \\ \hat{\delta}_2 \\ \hat{\delta}_3 \\ \hat{\delta}_4 \\ \hat{\delta}_5 \\ \hat{v}_1 \\ \hat{v}_2 \end{bmatrix} \tag{21}$$

$$\hat{v}_0 = \begin{bmatrix} 0 & 0 & 0 & 1 \end{bmatrix} \begin{bmatrix} \hat{\imath}_{L1} \\ \hat{\imath}_{L2} \\ \hat{v}_{C1} \\ \hat{v}_{C2} \end{bmatrix} \tag{22}$$

The general state-space model, which is provided in (23), can be recognised by comparing (21) and (22), and identified $\hat{A}$.

$$\left.\begin{aligned} \dot{\hat{x}} &= \hat{A}\hat{x} + \hat{B}\hat{u} \\ \hat{y} &= \hat{C}\hat{x} + \hat{D}\hat{u} \end{aligned}\right\} \tag{23}$$

The characteristics equation (CE) is $|\hat{A} - SI| = 0$. Where S is the LT variable and I is the unit-matrix of order 4×4.

$$S^4 + S^3 \frac{1}{RC_2} + S^2 \left(\frac{(d_1 + d_3 + d_5)^2}{C_1 L_2} + \frac{(1 - d_1 - d_3 - d_5)^2}{C_1 L_1} + \frac{1}{C_2 L_2}\right) + S\left(\frac{(d_1 + d_3 + d_5)^2}{RC_1 C_2 L_2} + \frac{(1 - d_1 - d_3 - d_5)^2}{RC_1 C_2 L_1}\right) +$$
$$\frac{1}{C_1 C_2 L_1 L_2}\big((1 - d_1 - d_3 - d_5)^2\big) = 0 \tag{24}$$

By comparing the (24) with $S^4 + S^3\alpha_1 + S^2\alpha_2 + S\alpha_3 + \alpha_4 = 0$. The Routh-Hurwitz stability criterion (RHSC) is used to determine the stability of the intended converter since the system has four orders, which eliminates the need for a pole-zero plot and the challenge of locating the poles and zeros of higher-order systems. The table of RHSC is seen below.

$$\begin{array}{c|ccc} S^4 & 1 & \alpha_2 & \alpha_4 \\ S^3 & \alpha_1 & \alpha_3 & 0 \\ S^2 & \dfrac{\alpha_1\alpha_2 - \alpha_3}{\alpha_1} & \alpha_4 & 0 \\ S^1 & \dfrac{\alpha_1\alpha_2\alpha_3 - \alpha_3{}^2 - \alpha_1{}^2\alpha_4}{\alpha_1\alpha_2 - \alpha_3} & 0 & 0 \\ S^0 & \alpha_4 & 0 & 0 \end{array}$$

The system maintains stability for all duty ratios below the allowable maximum, as indicated by the Routh-Hurwitz stability criterion. This is confirmed by the fact that all coefficients in (24) are positive, real, and non-zero, and all elements in the first column of the Routh-Hurwitz table are also positive.

3.   ANALYSIS AND DISCUSSION OF THE PROPOSED CONVERTER

In this article, the mathematical modelling of a CUK-based multi-input converter is presented, along with an analysis of its steady-state behavior. The performance of the proposed converter is evaluated through an experimental setup. The experimental validation of the proposed converter was carried out using a 250 W hardware prototype. The setup consists of two DC sources representing fuel cell and solar panel voltages (20 V and 12 V), connected through the converter to a 48 V output across a 10-ohm resistive load. The circuit uses four MOSFET switches (FQA38N30), diodes (MUR1560), inductors of 24 mH and 50 mH, and capacitors of 750 μF each. Switching is performed at 10 kHz using PWM signals generated through a microcontroller. Figure 4 shows the complete test setup, and component values are detailed in Table 1. Although simulations were performed during the design stage, they are not presented here due to paper length limitations. These results will be included in future work to complement the hardware findings. The gate signals applied to the four MOSFET switches, denoted as V_{GS1}, V_{GS2}, V_{GS3}, and V_{GS4} are illustrated in Figure 5(a). All switches operated at a consistent switching frequency of 10 kHz. Figure 5(b) displays the experimental waveforms of the inductor currents I_{L1} and I_{L2} along with the voltages across capacitors V_{C1}, V_{C2}. The measured RMS values were 18.19 A for I_{L1}, 6.38 A for I_{L2} and 47.74 V for the output voltage, with the peak output voltage reaching 56.32 V.

Figure 5(c) shows the voltage waveforms across the switches V_{GS1}, V_{GS2}, V_{GS3}, and V_{GS4}. The voltage stress experienced by switches S_1, S_2 and S_3, is found to be less than or approximately equal to the maximum input voltage. The stress on switch S_4 remains below twice the output voltage V_0, indicating that all switches operate within safe voltage limits. The input voltages V_1 and V_2 along with the output voltage V_0 and output current I_0 are depicted in Figure 5(d). The recorded values for V_1, V_2, V_0, and I_0 are 20 V, 12 V, and 47.74 V, 6.36 A respectively.
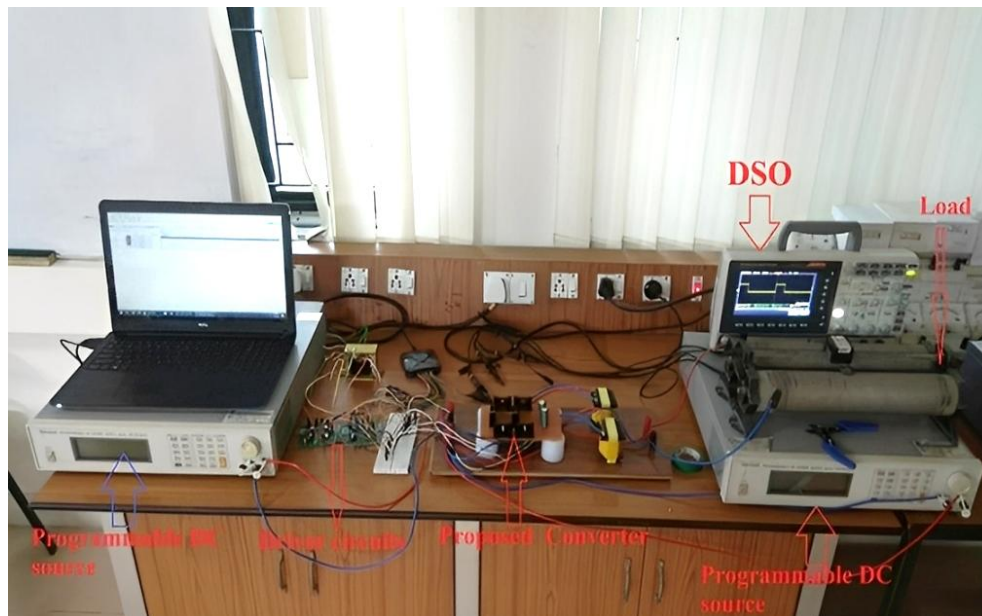

Figure 4. Experimental setup of CUK CUK-based novel multi-input converter

Table 1. Experimental setup

Parameter	Value
I/P Voltages	$V_1 = 20$ V, $V_2 = 12$ V
O/P Voltage	$V_0 = 48$ V
O/P Power	$P_0 = 250$ W
Switching frequency	10 KHz
Duty cycle $D_1 = D_2 = D_3$	0.33
Duty cycle D_4	0.72
Inductors	$L_1 = 24$ mH, $L_2 = 50$ mH
Capacitors	$C_1 = 750$ μF, $C_2 = 750$ μF
MOSFETs (4)	FQA38N30
Diode	MUR1560
Load	$R = 10$ Ω
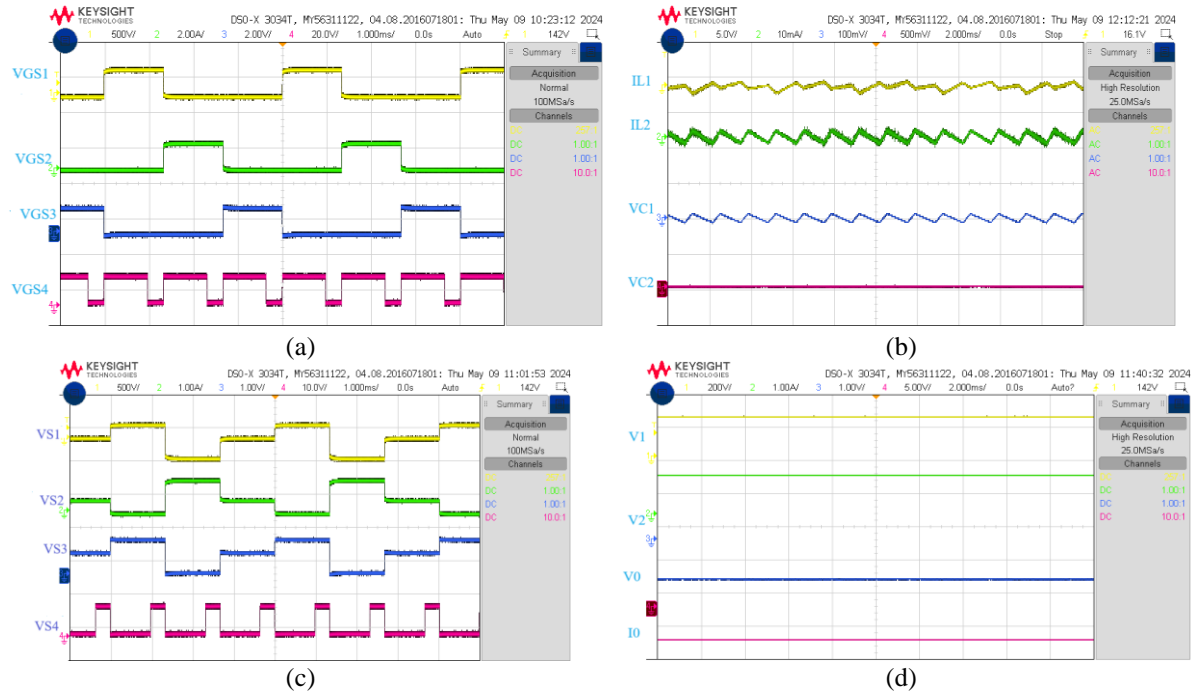
Figure 5. The prototype model experimental waveforms: (a) pulses of S_1, S_2, and S_3 and S_4,
(b) inductor currents and capacitor voltages, (c) voltage stress of S_1, S_2, and S_3, S_4 switches,
and (d) input and output voltages and output current

Compared to conventional CUK-based multi-input converters, the proposed topology offers several technical enhancements beyond the summarized metrics in Table 2. It achieves reduced component count, leading to a more compact and cost-effective design. The voltage stress across switches is significantly lower—especially on switch S4—enhancing device reliability. Unlike prior converters that employ relays or complex gating [16], [21], our design simplifies control due to symmetrical operating modes and consistent state-space models. The use of only three bidirectional switches minimizes losses while retaining full bidirectional power flow capability. Efficiency is maximized at 96.4%, outperforming most referenced designs operating below 95%. The system's non-isolated structure, with modular interfacing for fuel cells and PV sources, allows easier scalability for electric mobility platforms. This topology also ensures continuous input current and reduced output voltage ripple. These features collectively improve power management, reliability, and adaptability in hybrid low-power systems. Hence, the proposed converter stands out as a high-performance, application-specific solution for modern energy integration.

$$A_{11} = V_0 = \frac{(d_1 + d_2)V_1 + d_2 V_2}{1 - d_1 - d_2}$$

$$A_{12} = V_0 = \frac{d_1 V_1 + d_2(V_1 + V_2) + d_3 V_2}{1 - d_1 - d_2 - d_3}$$

$$A_{13} = V_0 = \frac{d_1 V_1 + (1 - d_1)V_2}{1 - d_2}$$

$$A_{14} = V_0 = -\frac{d_1 V_1 + d_2 V_2 + d_3(V_1 + V_2)}{1 - d_1 - d_2 - d_3}$$

$$A_{15} = V_0 = \frac{d_1 V_{battery} + (1 - d_1)V_1 + (1 - d_2)V_2}{1 - d_3}$$

$$A_{17} = V_0 = \frac{(2 - d_1)V_1 + V_2}{(1 - d_1)^2}$$

$$A_{18} = V_0 = \frac{(d_1 - 2d_2 + d_1 d_2)}{(1 - d_1)^2(d_1 - d_2)} V_1 + \frac{d_2(1 - d_1)}{d_1(d_1 - d_2)} V_2$$

$$A_{19} = V_0 = -\frac{d_1 + d_3 + d_5}{1 - d_1 - d_3 - d_5} \left(V_1(1 - d_3 - d_4) + V_2(1 - d_1 - d_2) \right)$$

Table 2. Comparing the proposed converter against current converters topologies

Topology	[15]	[16]	[17]	[18]	[19]	[20]	[21]	[22]	[23]	Proposed
Gain	A_{11}	A_{12}	A_{13}	A_{14}	A_{15}	A_{16}	A_{17}	A_{17}	A_{18}	A_{19}
Number of sources	2	2	2	2	3	2	2	2	2	2
Number of unidirectional switches	0	4	0	2	4	6	4	3	4	4
Number of capacitors	2	1	1	1	1	4	4	3	4	2
Number of inductors	2	1	1	1	1	4	4	3	4	2
Number of Bi-directional power switches	3	0	3	2	2	2	0	0	1	0
No. of diodes	5	3	1	0	2	2	4	3	1	1
No. of relays	0	4	3	0	0	0	0	0	0	0
Stress on voltage	High	-	-	High	Low	High	Moderate	Moderate	Moderate	Low
% efficiency	93.50	94	93	94	88-94	91	95	94	95	96.4

4. CONCLUSION

This work has presented the dynamic modelling and small-signal analysis of a bridge-type multi-input DC–DC converter developed for hybrid low-power systems. The converter enables continuous power delivery from two independent sources, providing enhanced operational flexibility. The design employs a CUK-based topology and multiple switching frequencies, which facilitate control over power flow and output regulation. The modelling approach includes steady-state analysis, average large-signal modelling, and small-signal representation, offering a detailed evaluation of the converter's behaviour. Experimental validation using a 250 W prototype confirms the theoretical predictions, achieving a peak efficiency of 96.4% with reduced voltage stress on the switching devices. In comparison with existing topologies, the proposed converter demonstrates improved performance and suitability for low-power applications.

Future work will focus on implementation of traditional and advanced controllers to improve the output voltage regulation. The converter's dynamic behavior under transient conditions will be analyzed using hardware-in-the-loop simulations. Scalability to medium and high-power applications will be explored through component and thermal redesign. Integration with lithium-ion batteries and supercapacitors will support regenerative braking. Real-time monitoring and smart grid compatibility will also be considered for enhanced control.

AUTHOR CONTRIBUTIONS STATEMENT

This journal uses the Contributor Roles Taxonomy (CRediT) to recognize individual author contributions, reduce authorship disputes, and facilitate collaboration.

Name of Author	C	M	So	Va	Fo	I	R	D	O	E	Vi	Su	P	Fu
Baya Reddy Lomada	✓	✓	✓	✓	✓	✓	✓	✓	✓	✓			✓	
Naga Bhaskar Reddy	✓	✓		✓		✓		✓		✓	✓	✓		

C : **C**onceptualization   I   : **I**nvestigation   Vi : **Vi**sualization
M : **M**ethodology   R   : **R**esources   Su : **Su**pervision
So : **So**ftware   D   : **D**ata Curation   P   : **P**roject administration
Va : **Va**lidation   O   : Writing - **O**riginal Draft   Fu : **Fu**nding acquisition
Fo : **Fo**rmal analysis   E   : Writing - Review & **E**diting

CONFLICT OF INTEREST STATEMENT
Authors state no conflict of interest.

DATA AVAILABILITY
Data availability is not applicable to this paper as no new data were created or analyzed in this study.

REFERENCES

[1] A. Midilli and I. Dincer, "Hydrogen as a renewable and sustainable solution in reducing global fossil fuel consumption," *International Journal of Hydrogen Energy*, vol. 33, no. 16, pp. 4209–4222, 2008, doi: 10.1016/j.ijhydene.2008.05.024.

[2] U. Mukherjee, E. Haghi, P. Prabhakaran, F. Graf, and M. Fowler, "Transitioning electricity systems: The environmental benefits and economic cost of repurposing surplus electricity in non-conventional end users," *International Journal of Hydrogen Energy*, vol. 44, no. 26, pp. 12891–12906, May 2019, doi: 10.1016/j.ijhydene.2019.03.173.

[3] R. Rapier, "Fossil fuels still supply 84 percent of world energy — and other eye openers from bp's annual review," *Forbes*. pp. 1–5, 2020. [Online]. Available: https://www.forbes.com/sites/rrapier/2020/06/20/bp-review-new-highs-in-global-energy-consumption-and-carbon-emissions-in-2019. (Accessed: July 20, 2021).

[4] R. Hannah and R. Max, "Energy production and consumption." 2021. [Online]. Available: https://ourworldindata.org/energy-production-consumption. (Accessed: November 8, 2021).

[5] U.S. Energy Information Administration, "Energy and the environment - where greenhouse gases come from." 2021. [Online]. Available: https://www.eia.gov/energyexplained/energy-and-the-environment/where-greenhouse-gases-come-from.php. (Accessed: October 21, 2021).

[6] B. Eisavi, F. Ranjbar, H. Nami, and A. Chitsaz, "Low-carbon biomass-fueled integrated system for power, methane and methanol production," *Energy Conversion and Management*, vol. 253, pp. 115163–115185, 2022, doi: 10.1016/j.enconman.2021.115163.

[7] Y. Budak and Y. Devrim, "Comparative study of PV/PEM fuel cell hybrid energy system based on methanol and water electrolysis," *Energy Conversion and Management*, vol. 179, pp. 46–57, 2019, doi: 10.1016/j.enconman.2018.10.053.

[8] A. A. Munshi and Y. A. R. I. Mohamed, "Extracting and defining flexibility of residential electrical vehicle charging loads," *IEEE Transactions on Industrial Informatics*, vol. 14, no. 2, pp. 448–461, 2018, doi: 10.1109/TII.2017.2724559.

[9] S. Bairabathina and S. Balamurugan, "Review on non-isolated multi-input step-up converters for grid-independent hybrid electric vehicles," *International Journal of Hydrogen Energy*, vol. 45, no. 41, pp. 21687–21713, 2020, doi: 10.1016/j.ijhydene.2020.05.277.

[10] C. E. Thomas, "Fuel cell and battery electric vehicles compared," *International Journal of Hydrogen Energy*, vol. 34, no. 15, pp. 6005–6020, 2009, doi: 10.1016/j.ijhydene.2009.06.003.

[11] G. Nicoletti, N. Arcuri, G. Nicoletti, and R. Bruno, "A technical and environmental comparison between hydrogen and some fossil fuels," *Energy Conversion and Management*, vol. 89, pp. 205–213, 2015, doi: 10.1016/j.enconman.2014.09.057.

[12] T. Capurso, M. Stefanizzi, M. Torresi, and S. M. Camporeale, "Perspective of the role of hydrogen in the 21st century energy transition," *Energy Conversion and Management*, vol. 251, pp. 114898–114914, 2022, doi: 10.1016/j.enconman.2021.114898.

[13] International Energy Agency, "The future of hydrogen." 2019. [Online]. Available: https://www.iea.org/reports/the-future-of-hydrogen. (Accessed: May 5, 2020).

[14] Alternative Fuels Data Center, U.S Department of Energy, "Hydrogen production and distribution." 2021. [Online]. Available: ttps://afdc.energy.gov/fuels/hydrogen_production.html. (Accessed: June 24, 2021).

[15] S. K. Haghighian, S. Tohidi, M. R. Feyzi, and M. Sabahi, "Design and analysis of a novel SEPIC-based multi-input DC/DC converter," *IET Power Electronics*, vol. 10, no. 12, pp. 1393–1402, 2017, doi: 10.1049/iet-pel.2016.0654.

[16] S. Kumaravel, G. G. Kumar, K. Veeranna, and V. Karthikeyan, "Novel non-isolated modified interleaved dc-dc converter to integrate ultracapacitor and battery sources for electric vehicle application," in *2018 20th National Power Systems Conference, NPSC 2018*, 2018. doi: 10.1109/NPSC.2018.8771810.

[17] G. G. Kumar, K. Sundaramoorthy, S. Athikkal, and V. Karthikeyan, "Dual input super boost DC-DC converter for solar powered electric vehicle," *IET Power Electronics*, vol. 12, no. 9, pp. 2276–2284, 2019, doi: 10.1049/iet-pel.2018.5255.

[18] S. Athikkal, G. Guru Kumar, K. Sundaramoorthy, and A. Sankar, "A non-isolated bridge-type dc-dc converter for hybrid energy source integration," *IEEE Transactions on Industry Applications*, vol. 55, no. 4, pp. 4033–4043, 2019, doi: 10.1109/TIA.2019.2914624.

[19] K. Varesi, S. H. Hosseini, M. Sabahi, and E. Babaei, "Performance analysis and calculation of critical inductance and output voltage ripple of a simple non-isolated multi-input bidirectional DC-DC converter," *International Journal of Circuit Theory and Applications*, vol. 46, no. 3, pp. 543–564, 2018, doi: 10.1002/cta.2392.

[20] K. Varesi, S. Hosseini, M. Sabahi, E. Babaei, S. Saeidabadi, and N. Vosoughi, "Design and analysis of a developed multiport high step-up DC-DC converter with reduced device count and normalized peak inverse voltage on the switches/diodes," *IEEE Transactions on Power Electronics*, vol. 34, no. 6, pp. 5464–5475, 2019, doi: 10.1109/TPEL.2018.2866492.

[21] K. Varesi, S. H. Hosseini, M. Sabahi, and E. Babaei, "Modular non-isolated multi-input high step-up dc-dc converter with reduced normalised voltage stress and component count," *IET Power Electronics*, vol. 11, no. 6, pp. 1092–1100, 2018, doi: 10.1049/iet-pel.2017.0483.

[22] K. Varesi, S. H. Hosseini, M. Sabahi, and E. Babaei, "A high-voltage gain non-isolated noncoupled inductor based multi-input dc-dc topology with reduced number of components for renewable energy systems," *International Journal of Circuit Theory and Applications*, vol. 46, no. 3, pp. 505–518, 2018, doi: 10.1002/cta.2428.

[23] Gaurav, N. Jayaram, S. Halder, K. P. Panda, and S. V. K. Pulavarthi, "A novel design with condensed component of multi-input high gain nonisolated dc–dc converter for performance enhancement in carbon neutral energy application," *IEEE Journal of Emerging and Selected Topics in Industrial Electronics*, vol. 4, no. 1, pp. 37–49, 2022, doi: 10.1109/jestie.2022.3211779.

[24] S. Jaganathan, B. Chandrasekar, and M. P. F. Queen, "Investigation of non-isolated dual-input step-up dc–dc converter using sliding mode control for ev application," *Electrical Engineering*, vol. 106, no. 4, pp. 4155–4170, 2024, doi: 10.1007/s00202-023-02172-z.

[25] D. W. Hart, *Power electronics*. Tata McGraw-Hill Education, 2011.

BIOGRAPHIES OF AUTHORS

Baya Reddy Lomada is currently serving as an assistant professor in the Department of Electrical and Electronics Engineering at Annamacharya Institute of Technology and Sciences (Autonomous), Rajampet, Andhra Pradesh, India. He is presently pursuing a Ph.D. in Electrical Engineering at JNTU College of Engineering, Anantapur. He holds an M.Tech. (Power Electronics and Drives) degree from the National Institute of Technology, Kurukshetra, and a B.Tech. (electrical and electronics engineering) degree from JNTU College of Engineering, Anantapur. His areas of research include power electronics, with a particular focus on DC–DC converters and their applications in hybrid electric vehicle systems. He can be contacted at email: reddy.baya@gmail.com.

Vangala Naga Bhaskar Reddy was born in Kurnool, India. He received the B.Tech. (Electrical and Electronic Engineering) degree from the Bangalore University, Bangalore, in 2000, M.Tech. (power electronics and drives) from the Bharath Institute of Higher Education Research [BIHER], Chennai, in 2005. He attained his Doctoral degree from Jawaharlal Nehru Technological University, Kakinada, in 2012. He is currently a professor & HOD of the Department of Electrical and Electronic Engineering, R.G.M. College of Engineering and Technology, Nandyal. His area of interest is power electronics, microcontrollers, and power electronic converters in hybrid electrical vehicle applications. He can be contacted at email: nagabhaskarreddy@rgmcet.edu.in.